

Supporting Information

Dual-Anion Chemistry Synchronously Regulating Solvation Structure and Electric Double Layer for Durable Zn Metal Anodes

Rong Huang^{a,†}, Jingwei Zhang^{a,†}, Wei Wang^a, Xiaohong Wu^b, Xuelong Liao^a, Tiantian Lu^a, Youzeng Li^a, Jialei Chen^a, Shan Chen^a, Yu Qiao^b, Qing Zhao,^{a,*} and Huan Wang^{a,*}

^aKey Laboratory of Advanced Energy Materials Chemistry (Ministry of Education), Renewable Energy Conversion and Storage Center (RECAST), Collaborative Innovation Center of Chemical Science and Engineering (Tianjin), College of Chemistry, Nankai University, Tianjin, 300071 China

^bState Key Laboratory of Physical Chemistry of Solid Surfaces, Department of Chemistry, College of Chemistry and Chemical Engineering, Xiamen University, Xiamen 361005, China.

*E-mail: huan.wang0520@nankai.edu.cn; zhaog@nankai.edu.cn

Experimental Section

Materials and Electrolyte Preparation

Zn foils (>99.99%) were purchased from Xinyi Metal Materials Co., Ltd. Zinc trifluoromethanesulfonate ($\text{Zn}(\text{OTf})_2$, >99%), zinc acetate ($\text{Zn}(\text{Ac})_2$, 99.99%) and zinc trifluoroacetate ($\text{Zn}(\text{TFA})_2$, 99.3%) were purchased from Adamas, Aladdin, and Bide Pharmatech Co., Ltd. respectively. Active carbon (AC) and VULCAN XC-72R carbon black were purchased from Kelude and Cabot, respectively. The electrolytes were prepared by mixing 2 moles $\text{Zn}(\text{OTf})_2$ salt with 0, 0.1, 0.7 moles $\text{Zn}(\text{Ac})_2$, and 0.7 moles $\text{Zn}(\text{TFA})_2$ in DI H_2O , and then fixing the solution volume, denoted as 2 OTf, 2F-01A, 2F-07A, 2F-07FA, respectively.

Electrode preparation

For coin-type Zn || AC supercapacitors, AC was mixed with Ketjenblack (Lion Corporation) and Polytetrafluoroethylene (PTFE, DuPont Chemours) at a weight ratio of 8:1:1 and dispersed in isopropanol (Macklin). Then the dough-like slurry was pressed onto carbon paper (Toray) disks (12 mm) and naturally dried in the air. The active mass loading is about 5 mg cm^{-2} , 12 mg cm^{-2} , and 18 mg cm^{-2} . For the Zn || AC pouch capacitor, AC was mixed with super P carbon black (SUPER P, TIMCAL) and polyvinylidene fluoride (PVDF, Sinopharm) at 8:1:1 weight ratio and dispersed in N-methyl-2-pyrrolidinone (NMP, Sinopharm), and then the slurry was coated on carbon paper (5 cm × 6 cm) and drying overnight at 80 °C in a vacuum oven with AC mass loading of 3 mg cm^{-2} . To fabricate the Zn-air battery, XC-72R was mixed with PTFE at a weight ratio of 9:1 and dispersed in isopropanol, and then the slurry was pressed onto carbon paper disks (12 mm) followed by naturally drying in the air with active mass loading of 9 mg cm^{-2} .

Material characterizations

Fourier Transform Infrared (FT-IR) analysis was conducted on Nicolet iS50. Raman spectroscopy was recorded on WITec alpha 300r laser confocal micro Raman system with an excitation wavelength of 532 nm. ^1H Nuclear magnetic resonance spectroscopy (^1H NMR), ^{17}O NMR and ^{65}Zn NMR spectra were collected by a Bruker Advance III 400MHz. Scanning electron microscopy (SEM) images and energy dispersive X-ray spectroscopy (EDS) mappings were collected using FEI Microscope (JSM-7900F). Transmission electron microscopy (TEM) and EDS mappings were performed on Talos F200X G2. X-ray diffraction (XRD) measurements were measured on a diffractometer (Smart Lab 9 KW) with a Cu-target X-ray tube ($\lambda=0.154 \text{ nm}$) at 150 mA and 40 kV. X-ray photoelectron spectroscopy (XPS, Axis Ultra DLD) used a monochromatic 1486.7 X-ray source. Time-of-Flight secondary ion mass spectrometry (ToF-SIMS) was carried out using IONTOF M6.

Electrochemical measurements

The Zn || Zn, Zn || Cu cells and Zn || AC capacitors were assembled using coin-type cells (CR2032) in the air with Zn foil (100 μm) as anodes, glass fiber (GF/D) as the separator, and Zn foil, Cu foil (30 μm) or AC as cathode, respectively. The Zn-air batteries were fabricated by custom mold with XC-72R as catalyst, and glass fiber (GF/A) as the separator. The cathode of Zn-air batteries was connected to air. Discharge/charge cycling performance was performed on a standard battery tester (LAND-CT2001A). A modified Aurbach method was utilized for the CE test consisting of a copper (Cu) foil (diameter: 12 mm) as the working electrode (substrate for Zn plating and stripping), and a Zn disk as the counter and reference electrode. A reservoir of 25 mAh cm^{-2} (Q_p) was applied to the Cu electrode at 5 mA cm^{-2} , and Zn stripping voltage was set as 0.5 V. After redepositing a Q_p of Zn onto Cu electrode, the cells underwent 10 times (n) stripping /plating (Q_c , 5 mAh cm^{-2}), followed by charging the cell to 0.5 V to strip the deposited Zn (Q_s , the stripped Zn capacity). The Aurbach CE was calculated by the equation:

$$\text{CE} = (10Q_c + Q_s) / (10Q_c + Q_p)$$

Linear sweep voltammetry (LSV), Tafel curves, CA, EIS, and CV were conducted on an electrochemical workstation (Ivium-Stat, Nederlanden). LSV of the investigated electrolytes was measured by three electrodes with Zn foil as the working electrode, Ti foil as the counter electrode, and saturated calomel electrode (SCE) as the reference electrode at a scan rate of 1 mV s^{-1} . The corrosion tests were conducted using three electrodes in different electrolytes with Zn foil as the working electrode and counter electrode, respectively, and SCE as the reference electrode at 1 mV s^{-1} . EIS was tested in the frequency range of 10^5 Hz to 10^{-2} Hz with a perturbation amplitude of 10 mV. The ionic conductivity of different electrolytes was measured by EIS via two parallel Pt-plate electrodes (1 cm × 1 cm). The distance between the two electrodes is 10 mm. The ionic conductivity of these electrolytes was calculated by the equation:

$$\sigma = L / (R_s \times A)$$

where σ is the ionic conductivity of the electrolyte (S cm^{-1}), and R_s is the electrolyte resistance (Ω), which corresponds to the intercept of the Nyquist plot. L is the distance between two Pt-plate electrodes (cm). A stands for the area of Pt electrode (cm^2).

Electric double layer capacitance (EDLC) was measured based on Zn|Zn symmetric cells at different scan rates (from 2 to 20 mV s⁻¹) in a voltage range of -0.015 to 0.015 V. The EDLC was calculated through the equation:

$$C = i/v$$

Where C and i represent capacitance and current, respectively. The value of i was determined by taking half of the current difference between positive and negative scans under each scanning rate.

Computational details

The DFT calculations on the adsorption energy of vacuum were performed using the Vienna Ab-initio Simulation Package (VASP).^{1, 2} The electron-ion interaction was described using the Projected Augmented-Wave (PAW) method, and the exchange-correlation interaction was computed using the Perdew-Burke-Ernzerhof (PBE) pseudopotential within the Generalized Gradient Approximation (GGA).^{3, 4} The van der Waals (vdW) interactions were calculated using the DFT-D3 method.⁵ The plane-wave energy cutoff was set to 400 electron volts. Convergence thresholds were set to 1.0×10⁻⁴ electron volts for energy and 0.05 electron volts/angstrom for forces. Brillouin zone sampling was performed using a 3×3×1 k-point grid. A vacuum layer of 20 angstroms was inserted in the z-direction to avoid interactions between periodic images.

The adsorption energy can be calculated according to the formula:

$$E_{\text{ad}} = E(\text{A+B}) - E(\text{A}) - E(\text{B})$$

where E_{ad} represents the adsorption energy, $E(\text{A+B})$ is the calculated energy of adsorption configuration, and $E(\text{A})$ and $E(\text{B})$ mean the calculated energy of substrate and adsorbent respectively.

Quantum chemistry (QC) calculations were conducted using Gaussian16,⁶ and molecular structures were visualized using Gaussview 6.0.⁷ This was done to investigate interactions between ions or molecules. The B3LYP functional was chosen for its robustness with the main group and transition elements. GD3(0) dispersion correction was applied to enhance the accuracy of weak interactions. A 6-311+G(d,p) basis set was used for C, H, O, S, and F atoms, while the Lanl2TZ basis set was applied for Zn atoms. In some cases, for more accurate atomic interaction calculations, refinement was performed using the M062X/6-311G+(d,p) method, including calculations of frontier orbital energies, electrostatic potential (ESP), and energy calculations, as well as HOMO and LUMO energy levels.^{7, 8}

Molecular dynamics (MD) simulations were carried out using Gromacs software⁹ to study the solvation behavior of electrolytes. The force field parameters for Zn²⁺ ions and the TIP3P water model were obtained from the Amber99SB force field. GAFF force field parameters for CH₃COO⁻, CF₃COO⁻, and CF₃SO₃⁻ anions were generated using the Acypype program. RESP atomic charges were used to describe electrostatic interactions, derived from RESP2 charges.¹⁰⁻¹² The number of salts and water molecules is detailed in Table S1. Gaussian 16 was employed to fit molecular electrostatic potentials at atomic centers to calculate atomic partial charges. The simulation process in the bulk phase involved energy minimization using the steepest descent method, followed by a 3 ns equilibration step using the Berendsen barostat. Subsequently, a 10 ns NPT run was conducted at a reference pressure of 1 bar, with a time step of 1 fs for analysis. Interface equilibrium simulations were performed in the NPT ensemble at 298 K and 1 bar, lasting 1 nanosecond, while production simulations were carried out in the NPT ensemble at 298 K for 50 nanoseconds. The number of salts, water molecules, and atoms of the Zn base is detailed in Table S2. A V-rescale thermostat at a reference temperature of 298 K was used. Electrostatic interactions were calculated using the particle mesh Ewald method, with a real space cutoff of 1.2 nm and a Fourier spacing of 0.12 nm. A Verlet cutoff scheme was employed to generate pair lists. A 1.2 nm cutoff was applied for non-bonded Lennard-Jones interactions. Periodic boundary conditions were applied in all directions, and hydrogen atoms were constrained. To validate equilibrium, the convergence of system energy, temperature, and box size was monitored. Gromacs was used to generate density profiles and radial distribution functions (RDFs), and VMD¹³ was employed to visualize the first solvation shell of Zn²⁺ ions during production simulations.

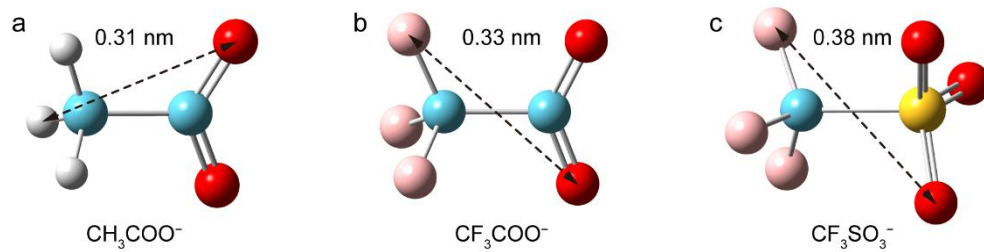


Figure S1. The configuration and size of (a) Ac^- , (b) TFA^- , and (c) OTf^- .

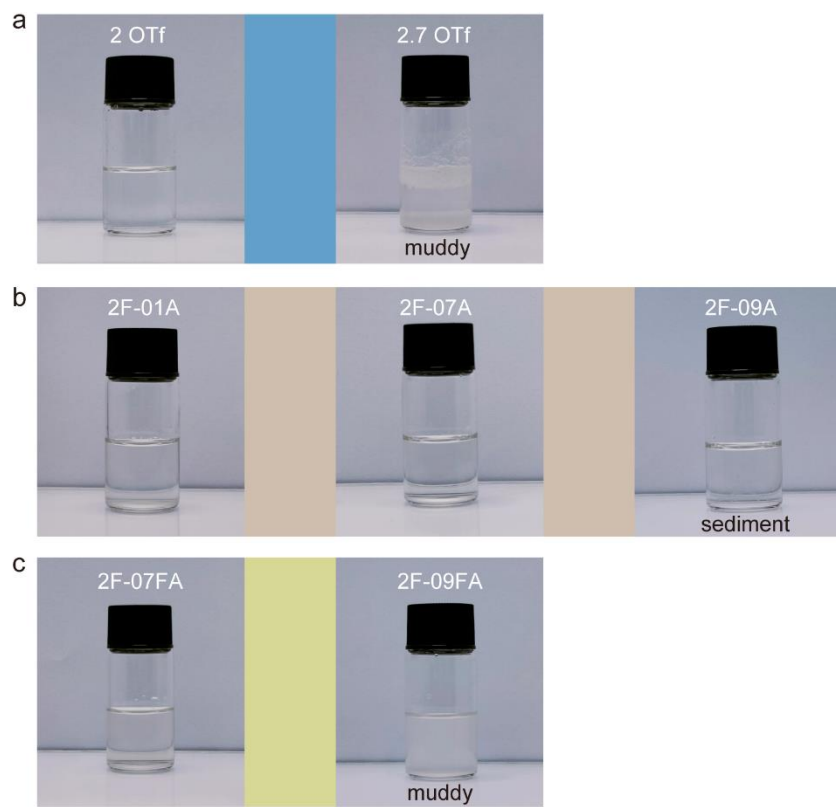


Figure S2. Photos of single and mixed salt solutions with different concentrations. (a) Single OTf⁻-based electrolytes. Different amounts of (b) Ac⁻ and (c) TFA⁻ incorporation into the baseline, respectively.

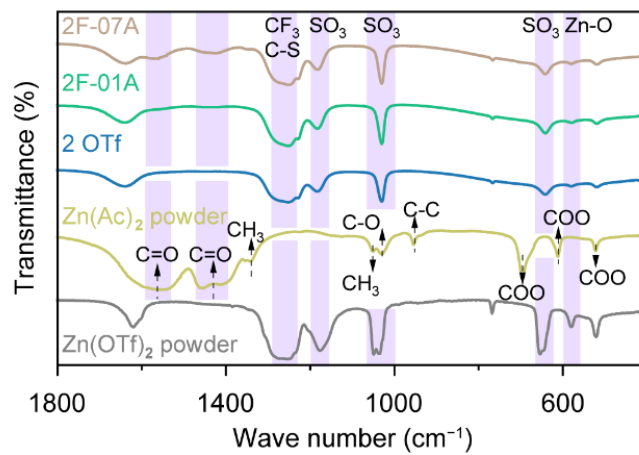


Figure S3. FTIR spectra of different electrolytes and pure $\text{Zn}(\text{Ac})_2$ and $\text{Zn}(\text{OTf})_2$ salts.

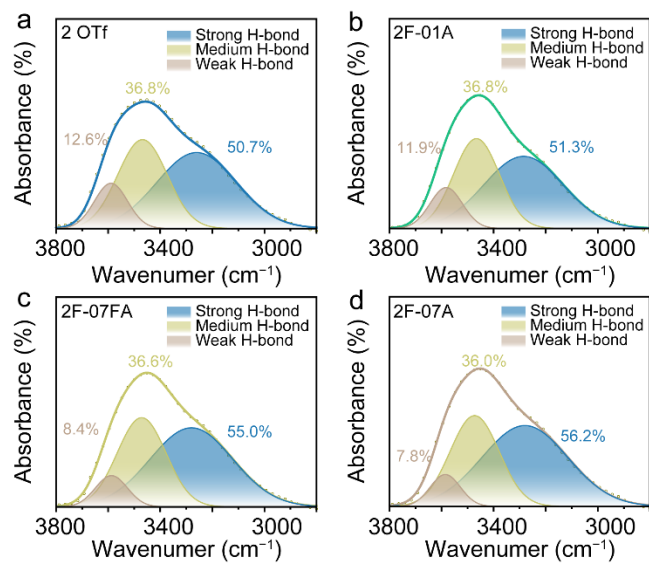


Figure S4. FTIR fittings of O-H stretching vibration of H₂O in (a) 2 OTf, (b) 2F-01A, (c) 2F-07FA, and (d) 2F-07A.

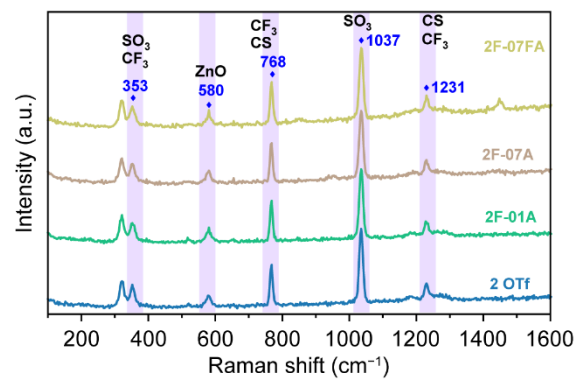


Figure S5. Raman spectra of different electrolytes to identify the characteristic peak.¹⁴

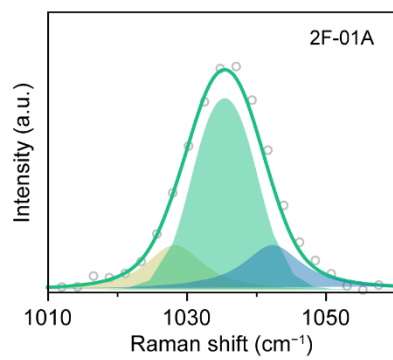


Figure S6. The fitted SO₃ stretching vibration in 2F-01A electrolyte.

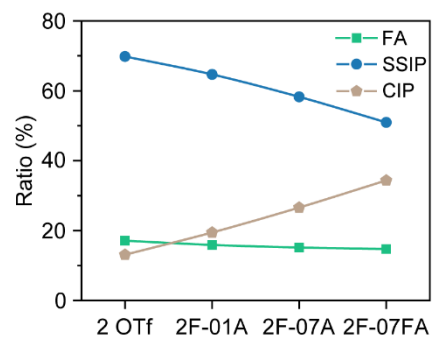


Figure S7. The FA, SSIP, and CIP ratios of the investigated electrolytes.

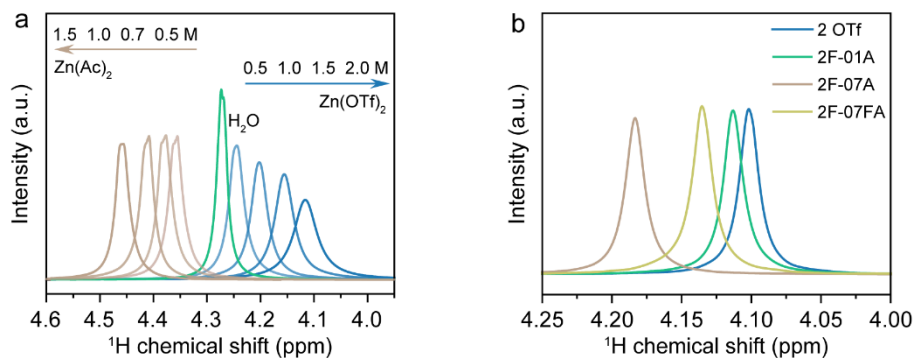


Figure S8. (a) ^1H NMR of aqueous $\text{Zn}(\text{Ac})_2$ and $\text{Zn}(\text{OTf})_2$ electrolytes with different concentrations. (b) ^1H NMR of 2F-07A, 2F-07FA, 2F-01A and 2 OTf.

The resonances of water protons shift downfield upon continuous addition of $\text{Zn}(\text{Ac})_2$ while shifting upfield in ^1H NMR is observed with increasing $\text{Zn}(\text{OTf})_2$ concentration (Figure S8a). The different changing trend in the chemical shift of H nuclei is ascribed to convertible hydrogen bond strength from $\text{Zn}^{2+}\text{-H}_2\text{O}$ and anion- H_2O pairs. With OTf^- introduction into H_2O , the H-bond networks of free H_2O were weakened, resulting in the shielding effect.¹⁵ As regulatory salts are added into H_2O and the baseline electrolyte, a downfield shift is observed due to the regulatory anions promoting the formation of strong H-bonds (Figure S8a-b).

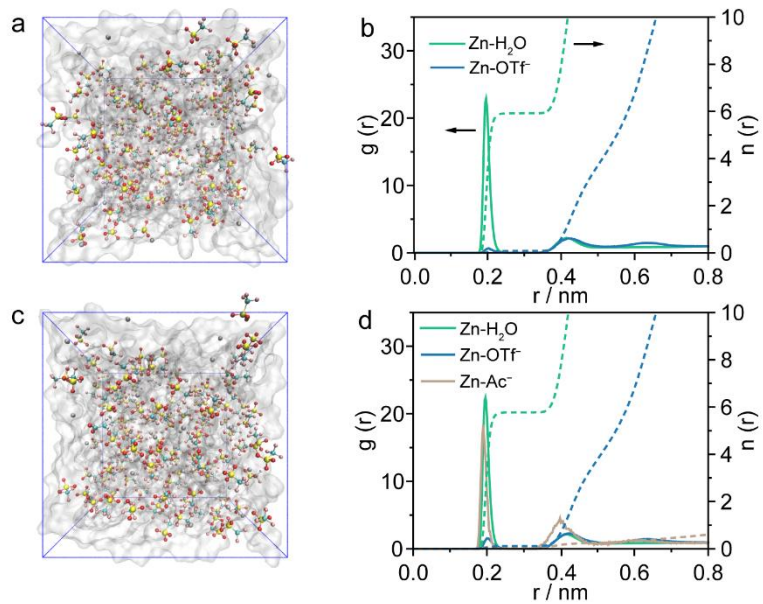


Figure S9. MD snapshots of (a) 2 OTf and (c) 2F-01A. RDFs and CN of (b) 2 OTf and (d) 2F-01A.

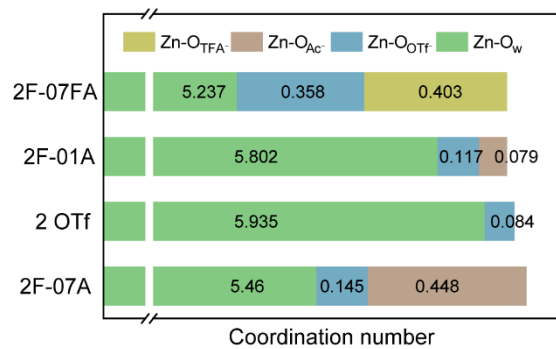


Figure S10. The coordination numbers of the Zn²⁺ complex within 0.3 nm in the investigated electrolytes.

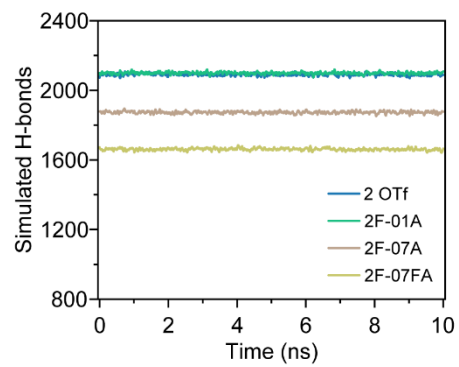


Figure S11. The simulated H-bonds of different electrolytes.

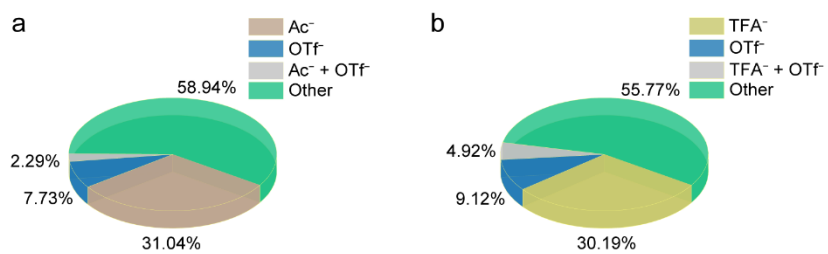


Figure S12. The statistical results of anions squeezed into the solvation sheath of Zn²⁺ in (a) 2F-07A and (b) 2F-07FA.

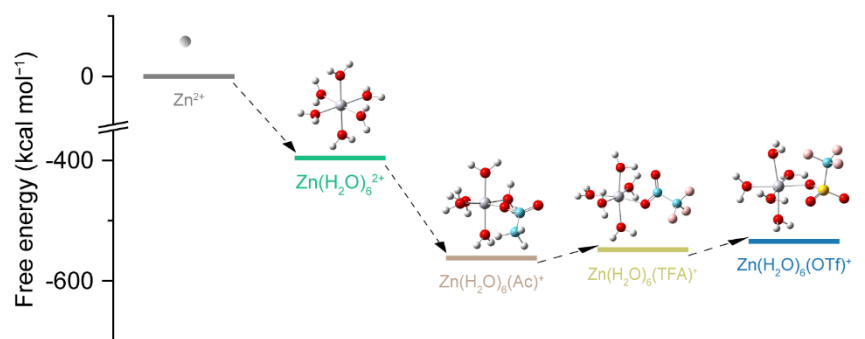


Figure S13. The Gibbs formation free energy of different solvation structures of Zn²⁺.

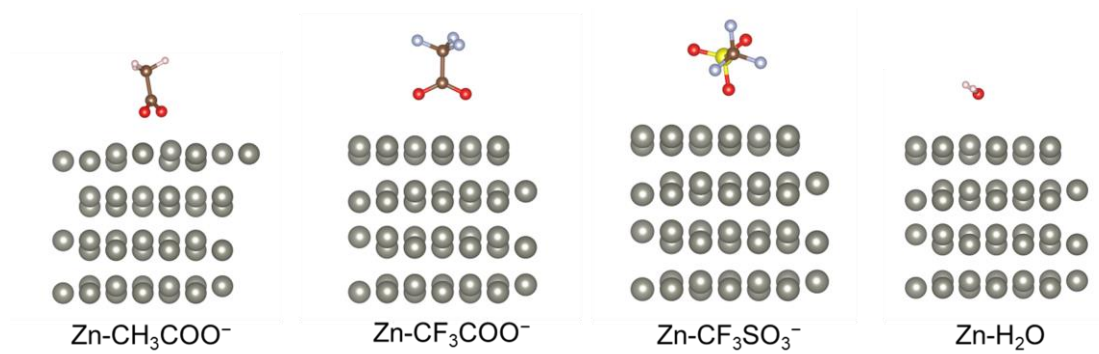


Figure S14. Adsorption energy models of different anions and water molecules on Zn (101) facet.

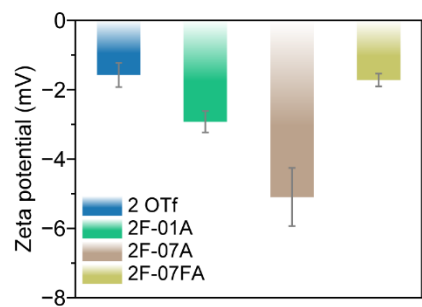


Figure S15. Zeta potential of Zn powder in different electrolytes.

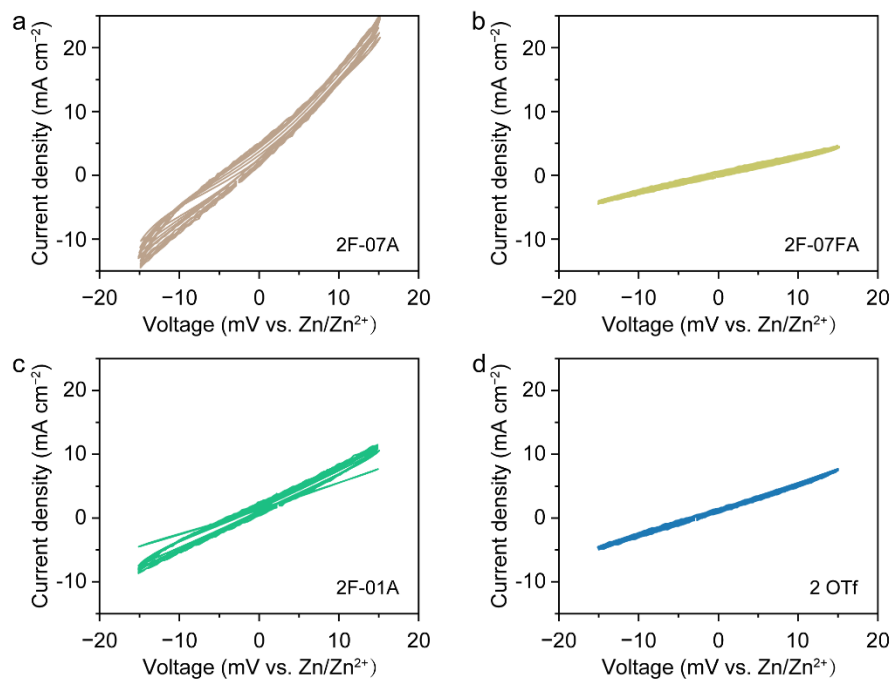


Figure S16. Cyclic voltammetry curves of Zn || Zn cells with (a) 2F-07A, (b) 2F-07FA, (c) 2F-01A, and (d) the baseline at different scan rates (from 2 to 20 mV s^{-1}) in a voltage range of -0.015 to 0.015 V.

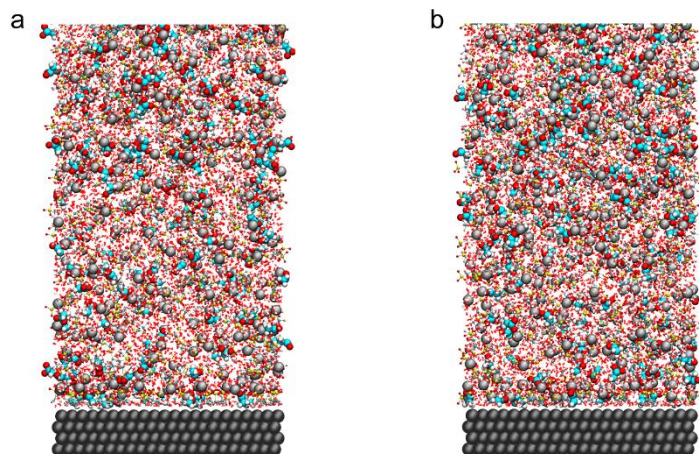


Figure S17. The side-view snapshots within EDL in 2F-07A at (a) initial state and (b) -100 mV.

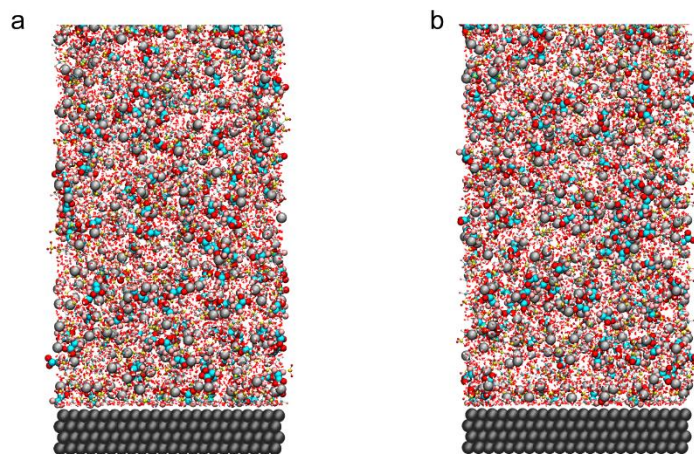


Figure S18. The side-view snapshots within EDL in 2F-07FA at (a) initial state and (b) -100 mV.

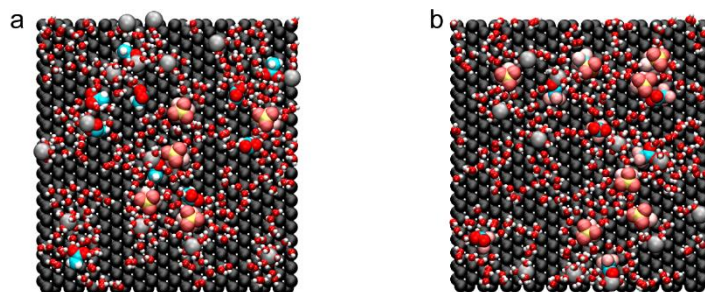


Figure S19. The top-view snapshots of the adsorbed species in the Helmholtz layer with (a) 2F-07A and (b) 2F-07FA under a bias voltage.

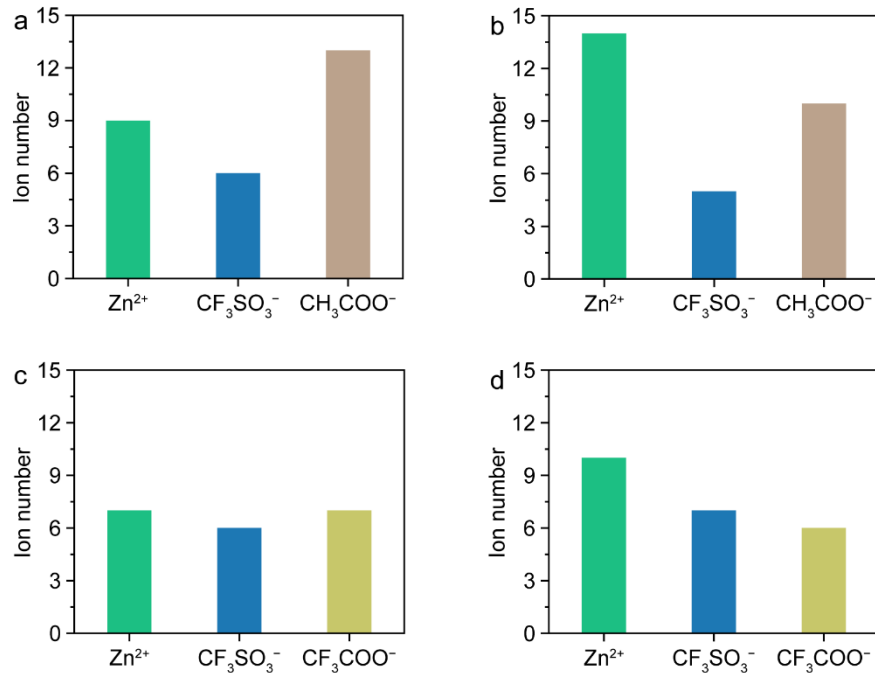


Figure S20. The amount of the ions in the Helmholtz layer of 2F-07A system at (a) initial state and (b) -100 mV, and that of 2F-07FA system at (c) initial state and (d) -100 mV.

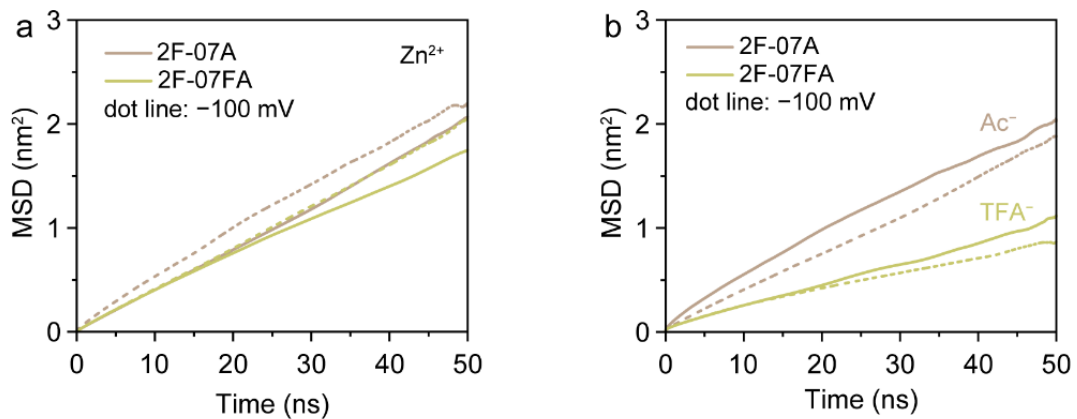


Figure S21. The mean square displacement (MSD) profiles of (a) Zn²⁺ and (b) regulatory anions with/without bias voltage.

The diffusion coefficient of different ions depends on the slope of MSD profiles with a greater slope corresponding to a higher diffusion coefficient. It is evident that the diffusion coefficient of Zn²⁺ and regulatory anions in 2F-07A system consistently surpasses that observed in 2F-07FA system with/without bias voltage.

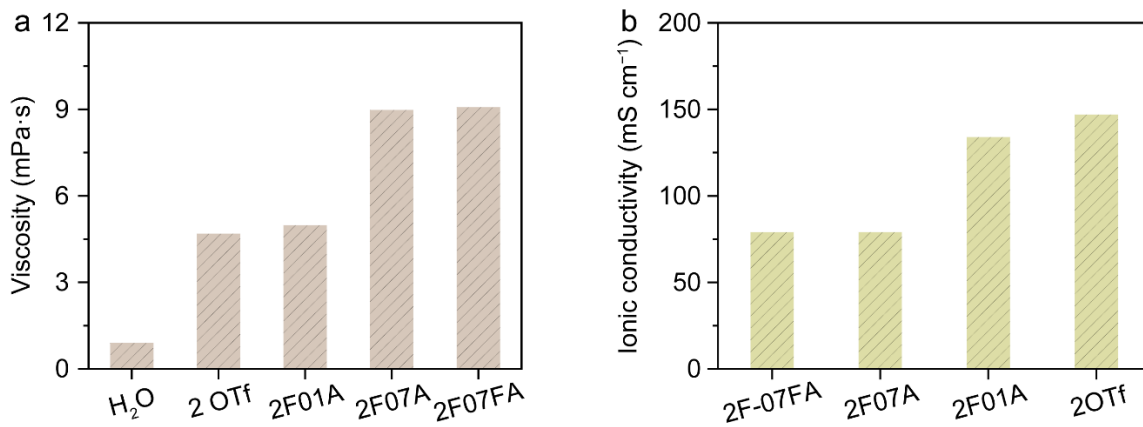


Figure S22. (a) Viscosity and (b) ionic conductivity of the examined electrolytes.

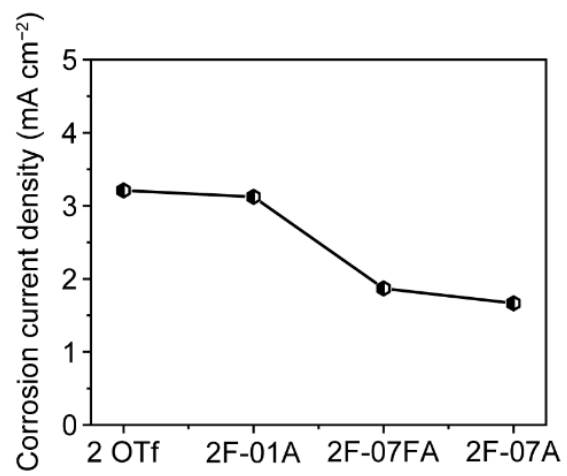


Figure S23. Corrosion currents of different electrolytes on Zn metal obtained *via* Tafel plots.

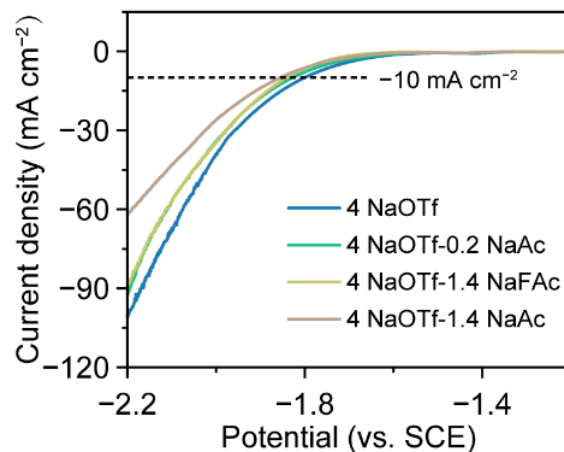


Figure S24. Linear sweep voltammetry characterization of HER in different anion-based electrolytes.

Linear sweep voltammetry was conducted to evaluate the activity of HER in these anion-based electrolytes without the competitive interference of Zn electroreduction. A more retarded potential of -1.86 V under an identical current density (-10 mA cm^{-2}) can be observed in 4 NaOTf-1.4 NaAc compared with 4 NaOTf-1.4 NaFAc (-1.84 V), 4 NaOTf-0.2 NaAc (-1.83 V), and 4 NaOTf (-1.79 V), further corroborating the superior HER-inhibition effect of the designed dual-anion electrolyte.

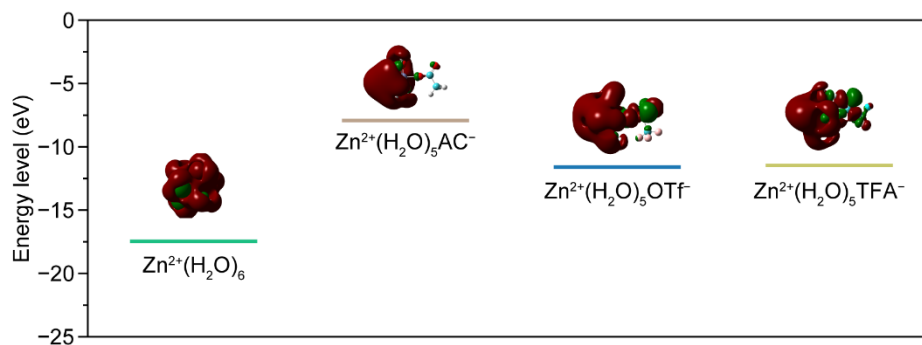


Figure S25. LUMO energy levels of different Zn^{2+} - H_2O -anion complexes.

The chemical origin of HER-inhibition in different Zn^{2+} - H_2O -anions complexes compared to fully hydrated Zn^{2+} was investigated by calculation of their LUMO energy levels. Previous works have demonstrated that the LUMO energy level of solvents can be decreased and increased by cations and anions, respectively.¹⁶ The LUMO of $\text{Zn}(\text{H}_2\text{O})_6^{2+}$ is pronouncedly reduced compared to free water, conducting predominant HER. The Zn^{2+} - H_2O -anions complexes in dual anion electrolytes harvest varying degrees of LUMO elevation and $\text{Zn}(\text{H}_2\text{O})_5(\text{Ac}^-)^+$ manifests the highest value amongst them, thus helping reduce water-related side reactions and incidental by-products.

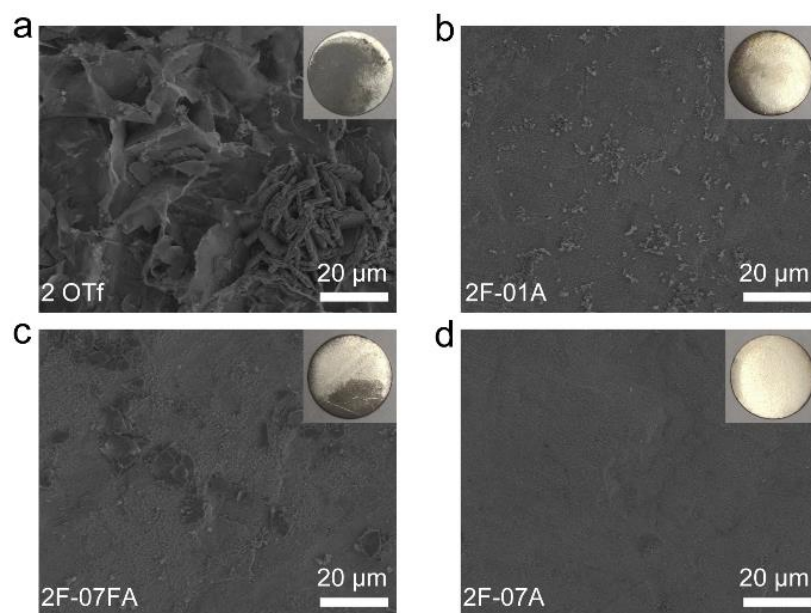


Figure S26. SEM images of the Zn plates after 100 h of immersion in (a) 2 OTf, (b) 2F-01A, (c) 2F-07FA, and (d) 2F-07A electrolytes. Inset: corresponding digital photos.

Figure S26 shows the surface morphology of Zn plates after immersion in different electrolytes for 100 h. Substantial by-product flakes are covered on the Zn plate with the baseline electrolyte, resulting in a dull gray color. In comparison, the lower density of by-products is observed in 2F-01A and 2F-07FA. While for 2F-07A, the Zn surface after 100 h of immersion is relatively smooth with negligible by-products. Thus, the tailored dual-anion electrolyte showcases the greatly improved anticorrosion ability.

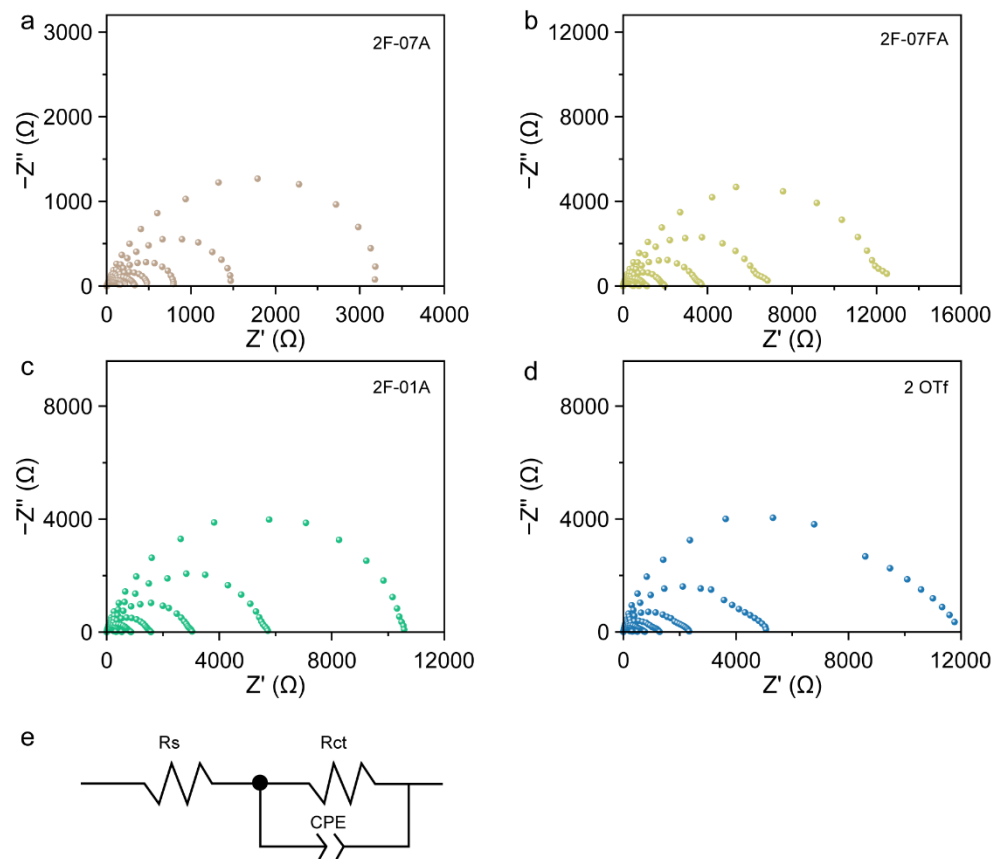


Figure S27. Temperature-dependent EIS tests of the symmetric Zn cells with (a) 2F-07A, (b) 2F-07FA, (c) 2F-01A, and (d) the baseline. (e) The equivalent circuit model.

The fitting results for R_{ct} are as follows:

	2 OTf	2F-01A	2F-07FA	2F-07A
	R_{ct} (Ω)			
273 K	12063.3	8791.3	12499.7	3184.9
283 K	5456.7	4490.8	7061.0	1478.4
293 K	2465.1	2430.4	3736.7	795.1
303 K	1333.7	1343.2	1970.1	488.1
313 K	780	771.9	1132.5	337.1
323 K	512.6	485.2	761.2	238.1
333 K	345.7	313.2	482.3	178.4

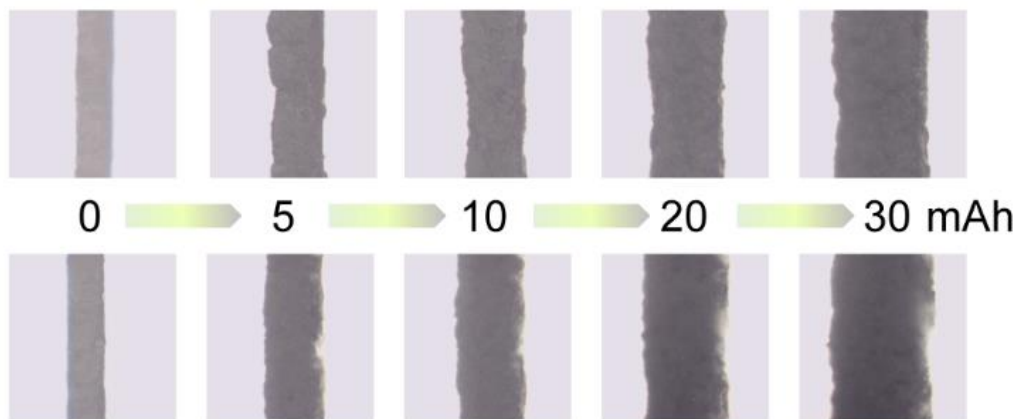


Figure S28. *In-situ* optical microscopy images of Zn plating process at a current density of 5 mA cm^{-2} in 2F-01A (top) and 2F-07FA (bottom).

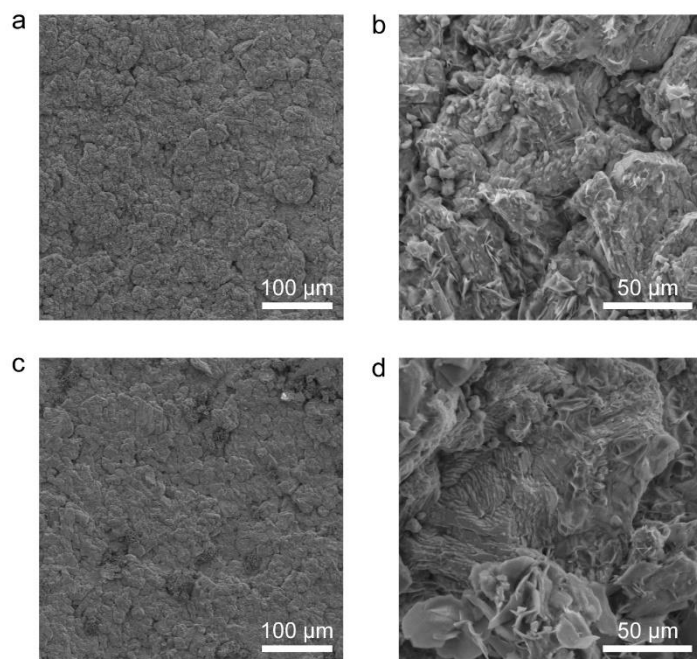


Figure S29. The deposition morphology after *in-situ* observation experiment in (a-b) 2F-01A and (c-d) 2F-07FA.

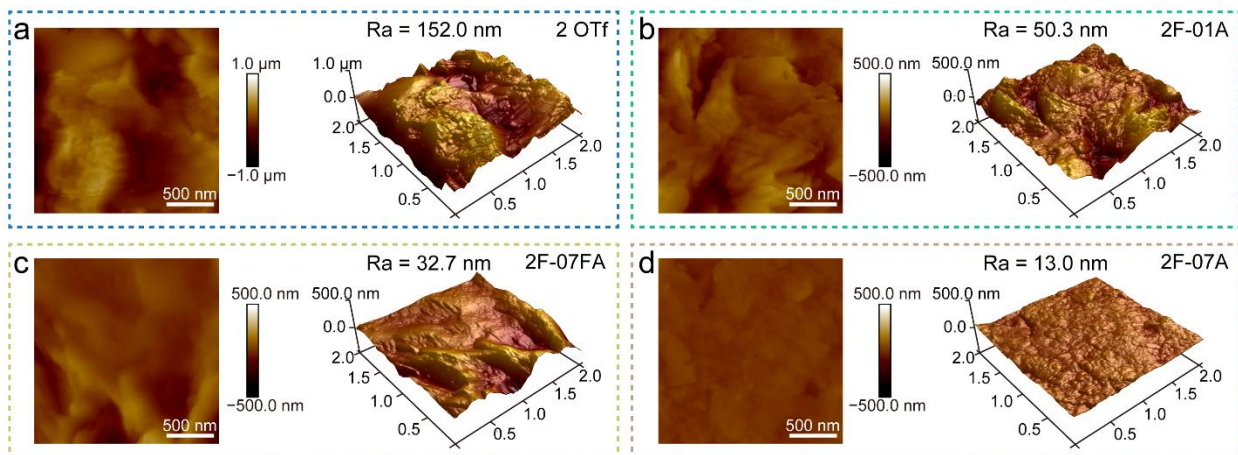


Figure S30. 2D (left) and 3D (right) AFM images of Zn electrodes after cycling at 5 mA cm^{-2} and 1 mAh cm^{-2} for 100 cycles in (a) 2 OTf, (b) 2F-01A, (c) 2F-07FA, and (d) 2F-07A.

AFM images of post-cycling Zn electrodes using different electrolytes are shown in Figure S30. Bulge and collapse appeared on the Zn surface in the baseline electrolyte, causing fluctuations in the micron scale with enormous surface roughness ($R_a = 152 \text{ nm}$) (Figure S30a), much higher than those in dual-anion electrolytes. In comparison to 2F-01A and 2F-07FA with vertical flakes detected on Zn surface (Figure S30b-c), 2F-07A based on synchronous regulation mechanism exhibits flat and dendrite-free deposition morphology with extremely low roughness ($R_a = 13.0 \text{ nm}$) (Figure S30d).

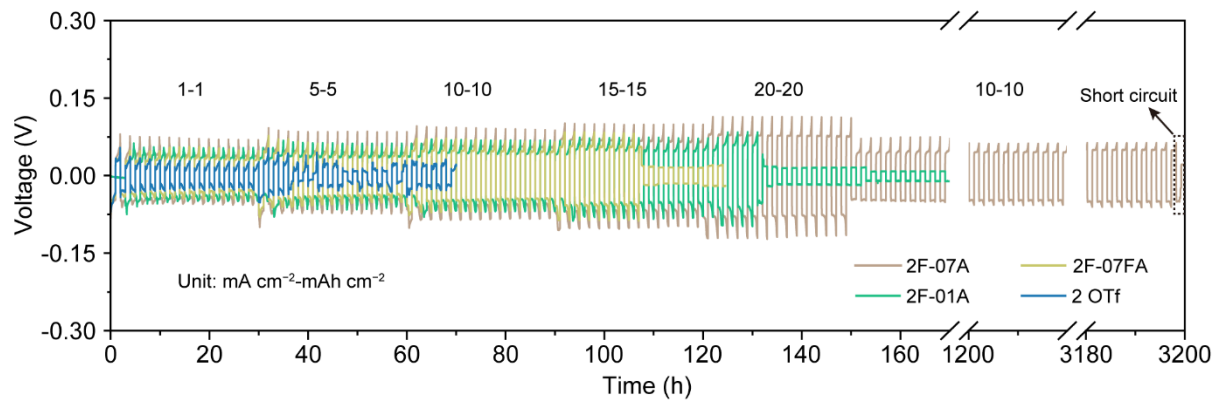


Figure S31. Zoomed-in voltage profiles of Zn||Zn cells at varying current densities and area capacities with different electrolytes.

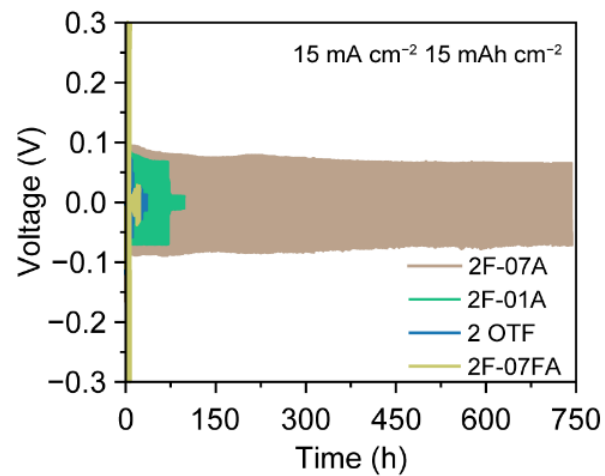


Figure S32. Galvanostatic plating/stripping voltage profiles of Zn||Zn cells at 15 mA cm⁻² and 15 mAh cm⁻² with different electrolytes.

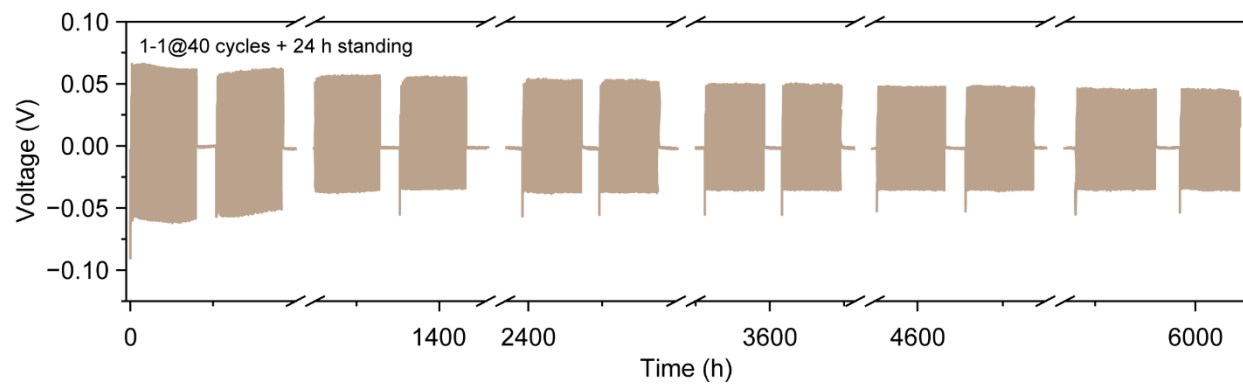


Figure S33. The intermittent test of Zn|Zn cell with 2F-07A electrolyte cycling at 1 mA cm^{-2} and 1 mAh cm^{-2} with 24 h interval.

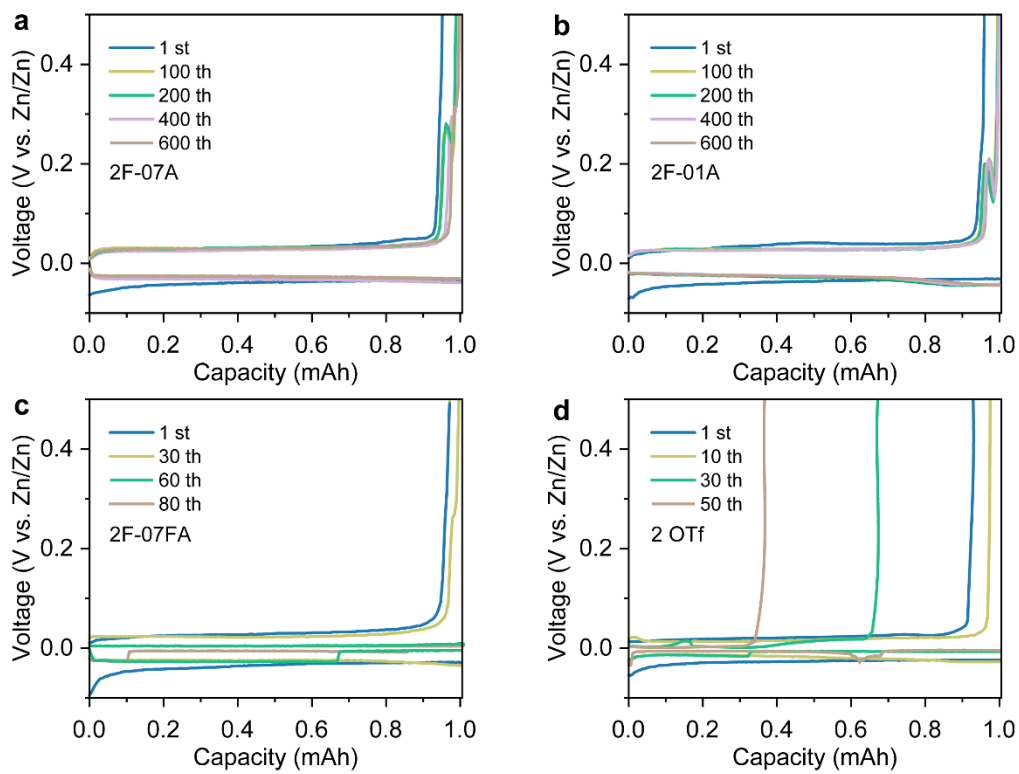


Figure S34. Voltage-capacity profiles of Zn|Cu asymmetric cells at 1 mA cm^{-2} and 1 mAh cm^{-2} in (a) 2F-07A, (b) 2F-01A, (c) 2F-07FA and (d) the baseline.

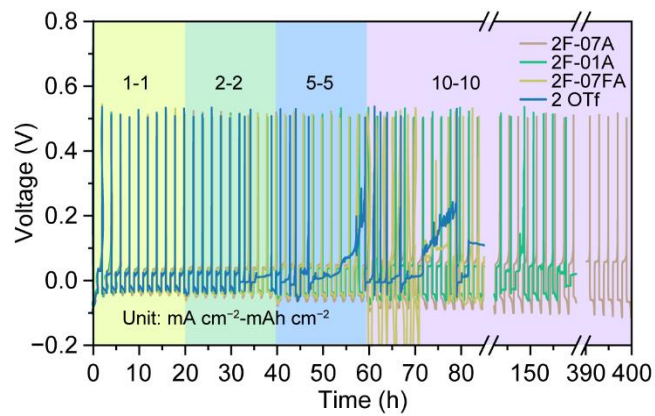


Figure S35. Voltage-time profiles of Zn||Cu asymmetric cells at varying current densities and area capacities.

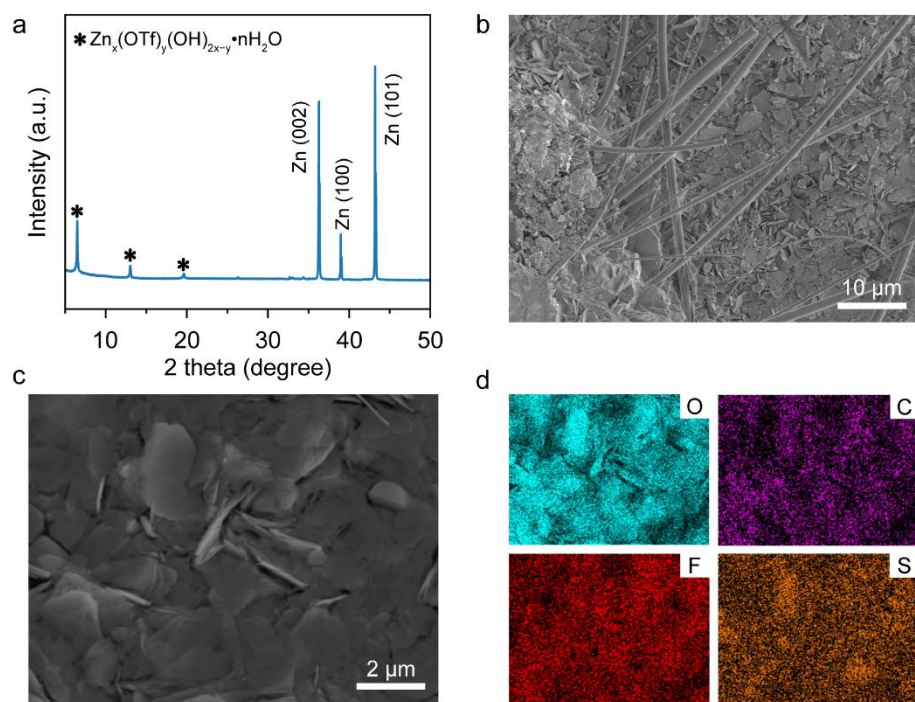


Figure S36. (a) XRD and (b) SEM image of Zn electrode after a short circuit in the baseline electrolyte. (c) SEM image of the selected area and (d) corresponding EDS mappings.

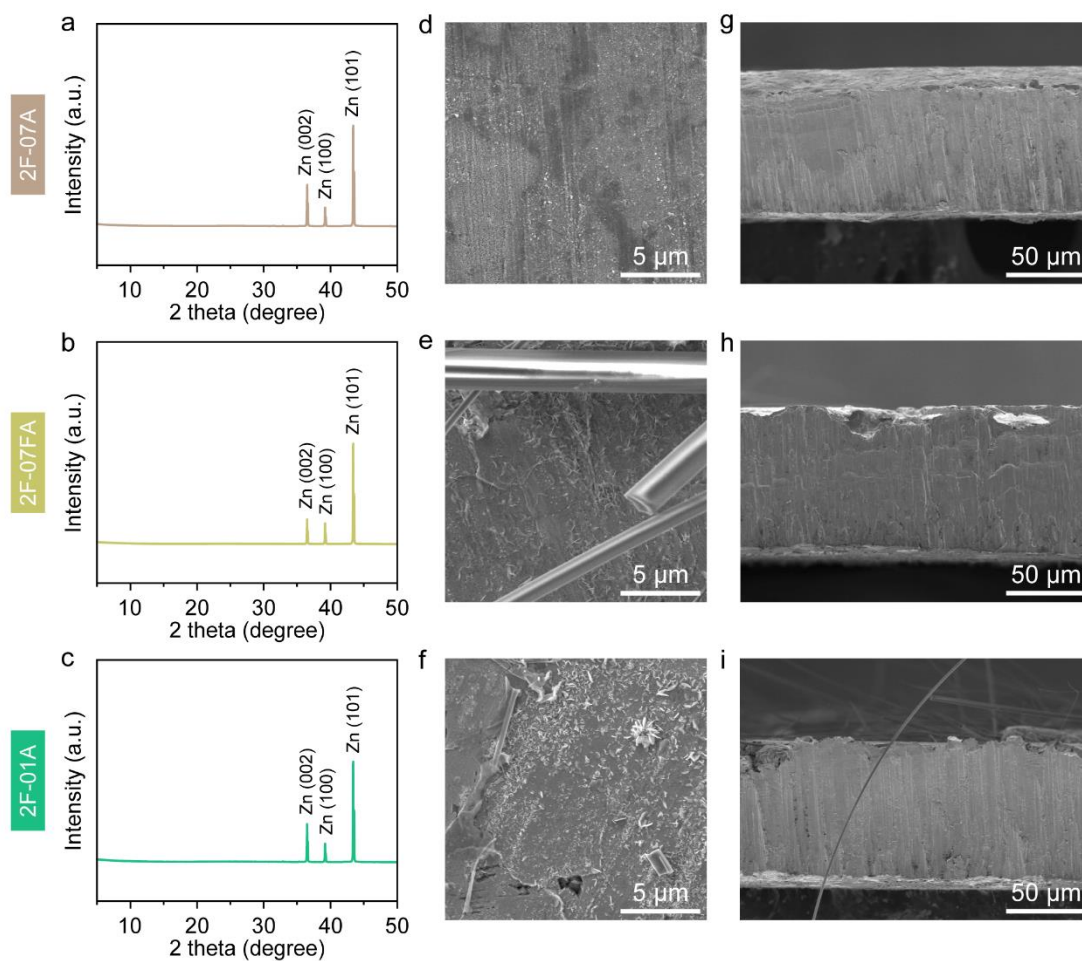


Figure S37. XRD patterns of Zn electrodes extracted from Zn||Zn cells after 50 cycles at 1 mA cm^{-2} and 1 mAh cm^{-2} in (a) 2F-07A, (b) 2F-07FA, and (c) 2F-01A. Top-view SEM images of those in (d) 2F-07A, (e) 2F-07FA, and (f) 2F-01A. Sectional SEM images of those in (g) 2F-07A, (h) 2F-07FA, and (i) 2F-01A.

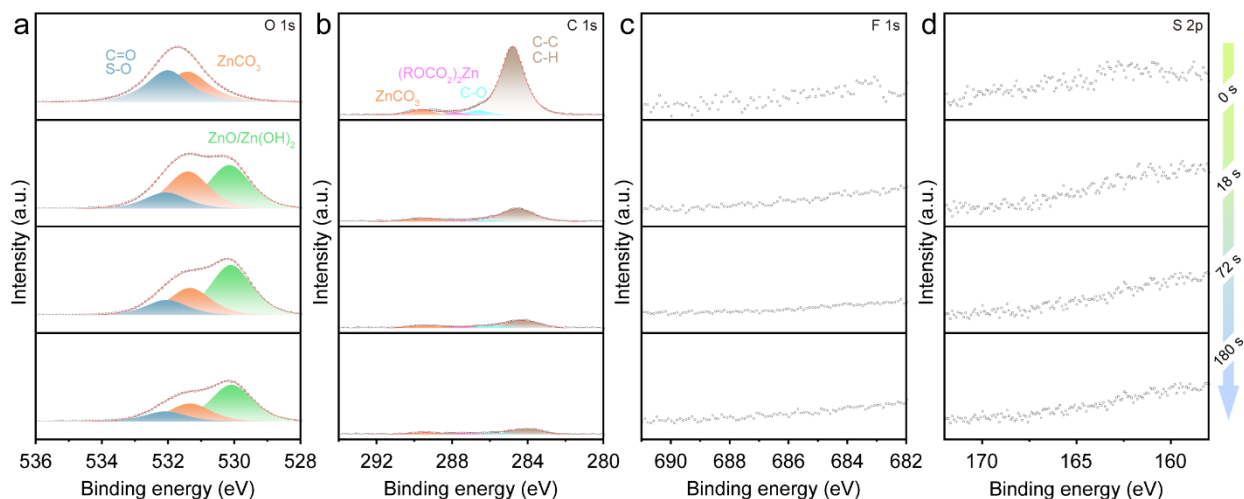


Figure S38. XPS depth profiles of (a) O 1s, (b) C 1s, (c) F 1s, and (d) S 2p for Zn electrodes extracted from 2F-01A electrolyte after 50 cycles at 1 mA cm^{-2} and 1 mAh cm^{-2} .

For O 1s spectra, it is dominated by organic species (S-O or C=O) at $\sim 532.8 \text{ eV}$ and ZnCO_3 at $\sim 532.2 \text{ eV}$ on the surface. A new peak assigned to ZnO/Zn(OH)_2 ($\sim 530.6 \text{ eV}$) appears after etching and gradually dominates the oxygen-containing components over 18 s of etching. For C 1s spectra, the ZnCO_3 signal at $\sim 290.0 \text{ eV}$ and $(\text{ROCO}_2)_2\text{Zn}$ at $\sim 288.5 \text{ eV}$ in 2F-01A electrolyte are both weaker than those in 2F-07A. More apparent differences can be observed in F 1s and S 2p spectra, where no F or S-related species can be detected in 2F-01A, confirming that a low concentration of Ac^- has weak capability in regulating the Zn^{2+} -solvation structure.

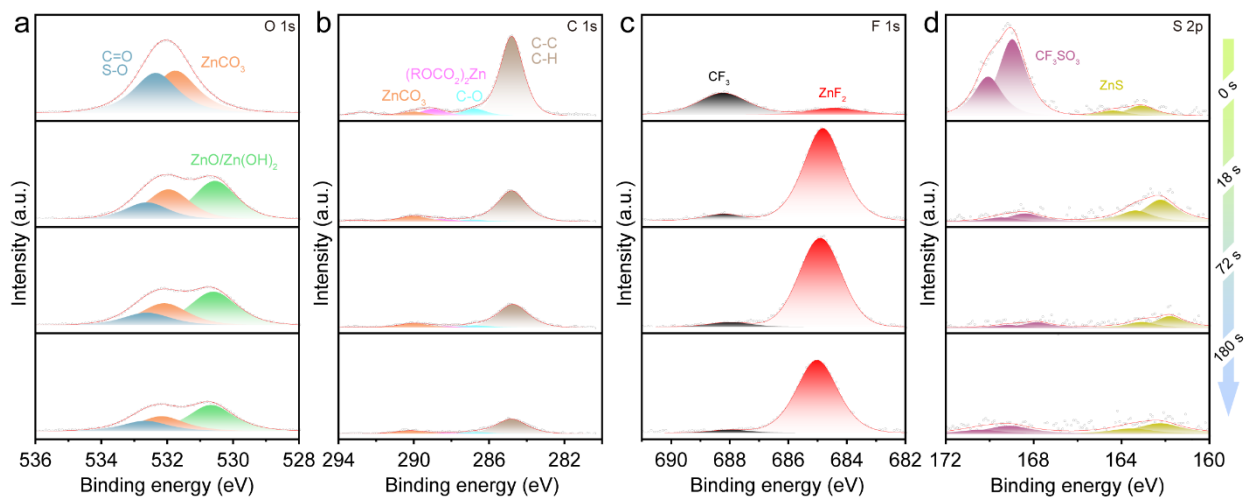


Figure S39. XPS depth profiles of (a) O 1s, (b) C 1s, (c) F 1s, and (d) S 2p for Zn electrodes extracted from 2F-07FA electrolyte after 50 cycles at 1 mA cm^{-2} and 1 mAh cm^{-2} .

For O 1s spectra, it is dominated by organic species (S-O or C=O) ($\sim 532.8 \text{ eV}$) and ZnCO_3 ($\sim 532.2 \text{ eV}$) on the surface. The peak assigned to ZnO/Zn(OH)_2 ($\sim 530.6 \text{ eV}$) emerges after etching and predominates the oxygen-containing components over 18 s of etching. In C 1s spectra, the ratio of ZnCO_3 ($\sim 290.0 \text{ eV}$) to $(\text{ROCO}_2)_2\text{Zn}$ ($\sim 288.5 \text{ eV}$) increases with the sputtering depth. For F 1s spectra, the ZnF_2 ($\sim 684.7 \text{ eV}$) gradually becomes a major component with extended sputtering time compared to organic $-\text{CF}_3$ ($\sim 688.4 \text{ eV}$). For S 2p spectra, the inorganic component of ZnS ($\sim 162.4 \text{ eV}$) also becomes predominated along with the decrease of $-\text{CF}_3\text{SO}_3$ species at $\sim 169.5 \text{ eV}$. Note that the ZnS signal in 2F-07FA is weaker than that in 2F-07A, largely due to the formation of non-uniform SEI in 2F-07FA.

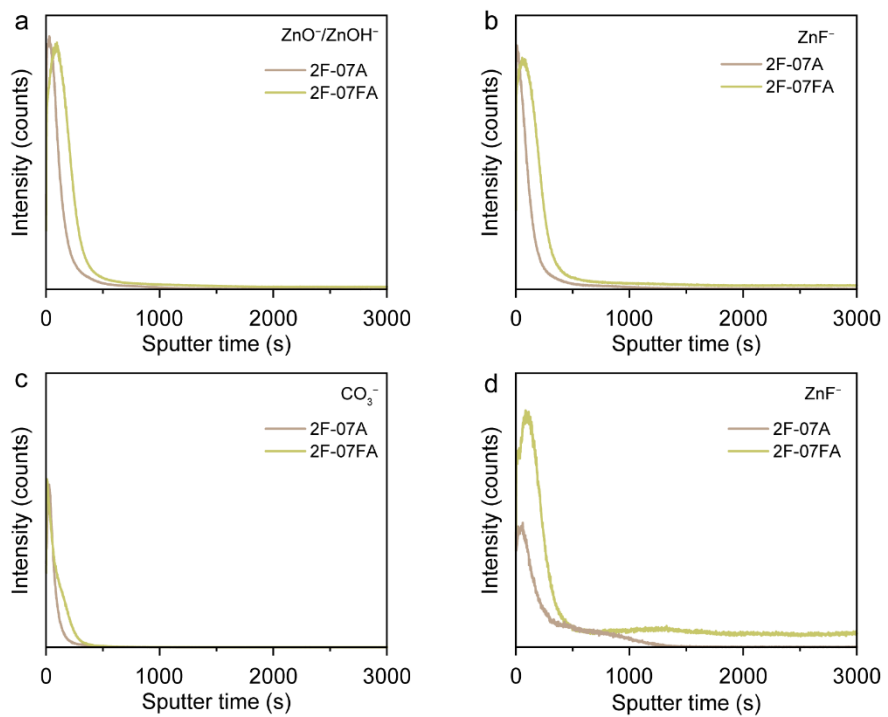


Figure S40. ToF-SIMS depth profiles of (a) ZnO⁻/ZnOH⁻, (b) ZnF⁻, (c) CO₃⁻ and (d) S⁻ with 3000 s etching of Zn electrodes in 2F-07A and 2F-07FA electrolyte after 50 cycles at 1 mA cm⁻² and 1 mAh cm⁻².

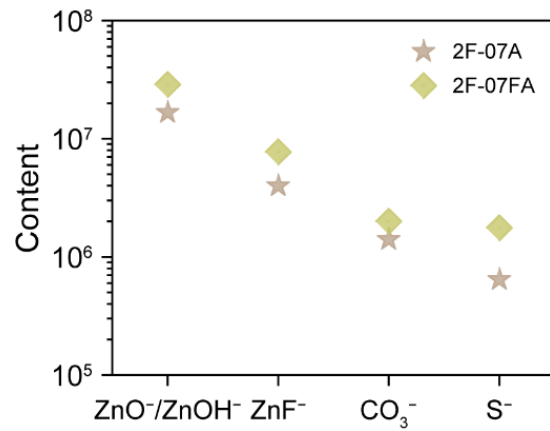


Figure S41. The second ion contents of SEI derived from ToF-SIMS depth profiles with 2F-07A and 2F-07FA electrolytes.

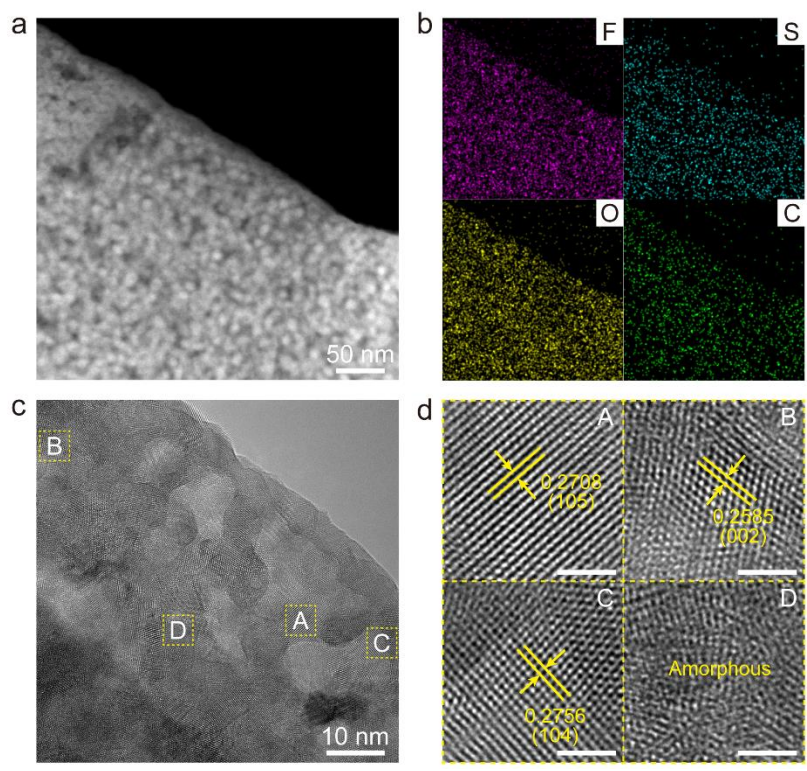


Figure S42. (a) HADDF TEM image. (b) Elemental mapping images. (c) HRTEM images of the SEI in 2F-07A electrolyte and (d) corresponding enlarged area images, scale bar: 2 nm.

Preliminary to TEM testing, a copper microgrid was inserted between Zn electrode and separator, followed by cycling at 1 mA cm^{-2} and 1 mAh cm^{-2} . After 50 cycles, the grid was extracted and washed with DI water for subsequent TEM imaging. A high-angle ring dark field (HADDF) image of the SEI layer derived from 2F-07A is revealed in Figure S42a. EDS elemental mappings demonstrate the even distribution of F, S, O, and C (Figure S42b). The component distribution of the SEI layer was elucidated using high-resolution TEM (HRTEM) (Figure S42c-d). A variety of domains with a clear lattice comprising Zn(OH)_2 (105), ZnF_2 (002), ZnCO_3 (104), and amorphous region are marked out.

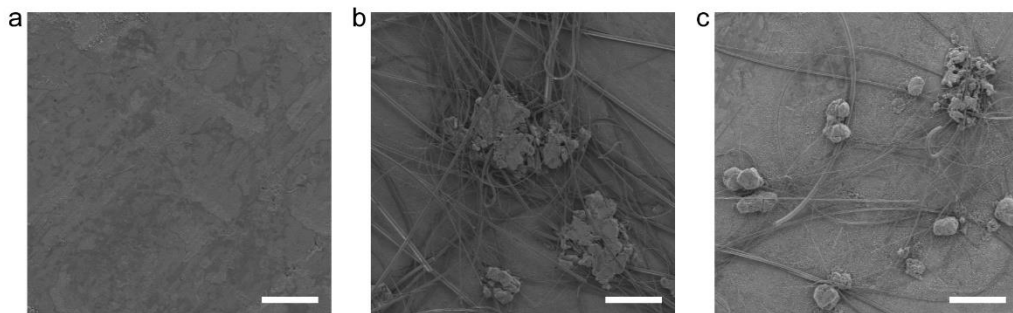


Figure S43. The surface morphology of the Zn anode retrieved from rate test with (a) 2F-07A, (b) the baseline, and (c) 2F-07FA. Scar bar: 50 μm .

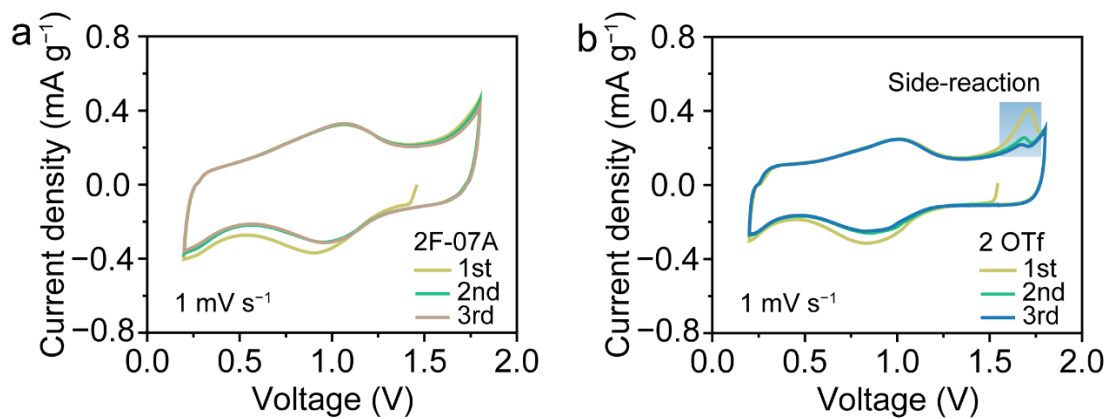


Figure S44. CV curves of Zn||AC hybrid capacitors at 1 mV s⁻¹ in (a) 2F-07A and (b) the baseline electrolyte.

In 2F-07A, the Zn||AC hybrid capacitor exhibits typical capacitor storage behavior and maintains good curve overlap after the first cycle (Figure S44a). While in the baseline electrolyte, side-reaction occurs during charging which in return affects the cycling stability (Figure S44b).

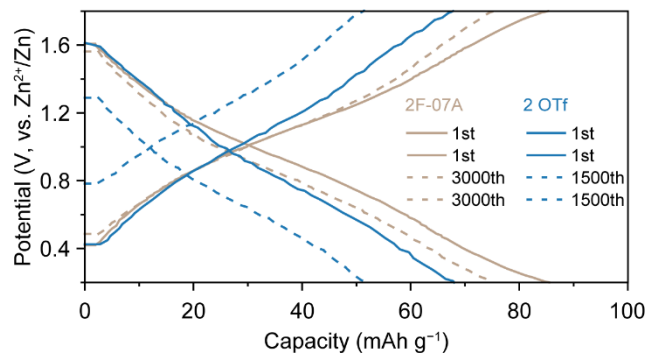


Figure S45. Galvanostatic discharging/charging voltage profiles of Zn||AC hybrid capacitors in 2F-07A and the baseline electrolytes at 1 A g⁻¹.

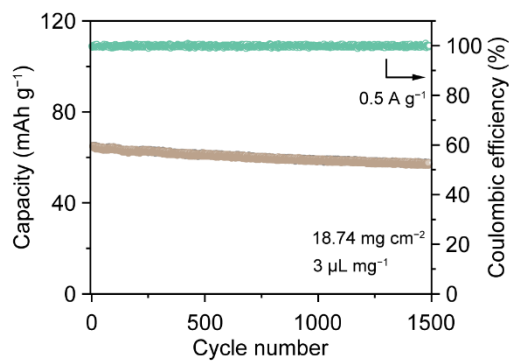


Figure S46. Long-term galvanostatic discharging/charging cycles of Zn²⁺ hybrid capacitors with high-loading AC cathode (18.74 mg cm⁻²) and lean 2F-07A electrolyte (3 μL mg⁻¹) at 0.5 A g⁻¹.

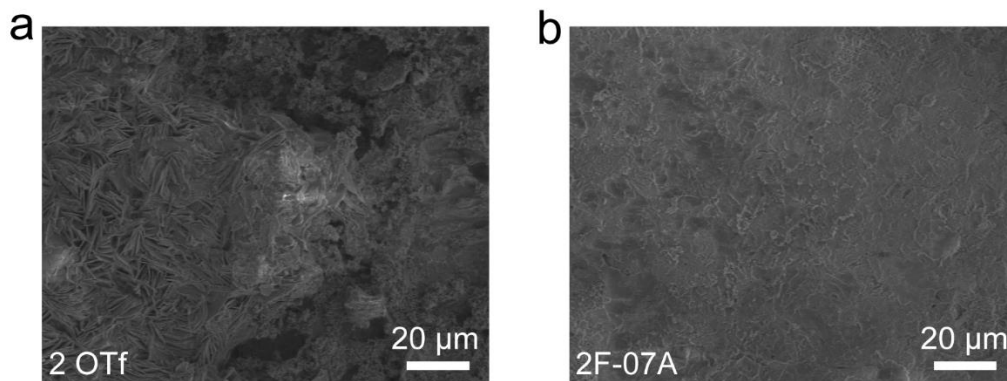


Figure S47. SEM images of Zn anode after cycling at 60 °C in Zn-air batteries using (a) the baseline electrolyte and (b) 2F-07A.

The postmortem analysis of Zn anode in Zn-air batteries after 240 h (2F-07A) and 180 h (2 OTf) cycling at 60 °C is shown in Figure S47. In the baseline electrolyte, the Zn anode suffers severe damage, where corrosion pits and dendrites are observed (Figure S47a). In sharp contrast, the Zn anode in 2F-07A maintains a comparatively complete and flat surface (Figure S47b).

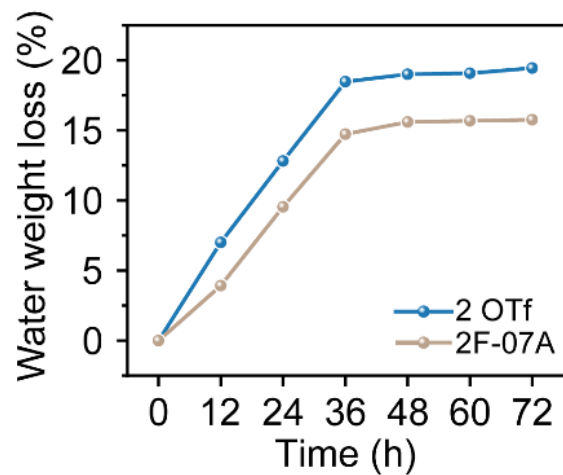


Figure S48. Water retention test of 2F-07A and the baseline electrolyte.

The water retention tests were carried out by measuring the water weight loss based on an open system. As shown in Figure S48. The optimized dual-anion electrolyte of 2F-07A demonstrates superior water retention capability owing to strong interactions between ions and H₂O.

Supplementary Table

Table S1. The number of solvents and ions used for bulk MD simulation.

Electrolyte composition	H ₂ O	Zn ²⁺	CF ₃ SO ₃ ⁻ (OTF ⁻)	CH ₃ COO ⁻ (Ac ⁻)	CF ₃ COO ⁻ (TFA ⁻)
2F-07A	1080	81	120	42	/
2F-01A	1200	63	120	6	/
2F-07FA	900	81	120	/	42
2 OTf (baseline)	1200	60	120	/	/

Table S2. The number of solvents, atoms, and ions used for interfacial MD simulation.

Electrolyte composition	H ₂ O	Zn ²⁺	CF ₃ SO ₃ ⁻ (OTF ⁻)	CH ₃ COO ⁻ (Ac ⁻)	CF ₃ COO ⁻ (TFA ⁻)	Zn base
2F-07A	5624	441	652	228	/	1760
2F-07FA	5567	441	652	/	228	1760

Table S3. The summary of cycling performance with respect to current density, area capacity, and calculative capacity of this work with those recently reported works.

Electrolyte regulation	Current density- Area capacity [mA cm ⁻² , mAh cm ⁻²]	Cycle life [h]	Calculative capacity [mAh cm ⁻²]	Reference
Poly(acrylamide-co-methyl acrylate)	5-5	2500	6250	1 ¹⁷
	10-10	780	3900	
	20-20	295	2950	
1-butyl-3-methylimidazolium cation	5-5	1400	3500	2 ¹⁸
	10-10	1000	5000	
Dimethylacetamide and trimethyl phosphate	5-5	1600	4000	3 ¹⁹
3-(1-methylimidazole) propanesulfonate	5-5	400	1000	4 ²⁰
	10-20	350	1750	
Sulolane	10-10	300	1500	5 ²¹
	40-10	160	3200	
12-crown-4	5-10	1700	4250	6 ²²
γ -butyrolactone	5-5	1250	3125	7 ²³
Zinc perfluoro(2-ethoxyethane)	2.5-5	380	475	8 ²⁴
Ammonium acetate	10-10	650	3250	9 ²⁵
	20-5	450	4500	
	20-20	120	1200	
	40-5	350	7000	
Saccharin	10-10	550	2750	10 ²⁶
Sodium 3,3'-dithiodipropene sulfonate	5-5	870	2175	11 ²⁷
Benzyltrimethylammonium chloride	10-5	500	2500	12 ²⁸
Xylitol and graphene oxide	30-30	87	1305	13 ²⁹
Lithium nitrate and dimethyl carbonate	10-10	1600	8000	14 ³⁰
Ac ⁻ -containing dual anion chemistry	10-10	3050	15250	This work
	15-15	742	5565	

References

1. G. Kresse and J. Furthmüller, *Phys. Rev. B*, 1996, **54**, 11169-11186.
2. G. Kresse and J. Furthmüller, *Comput. Mater. Sci.*, 1996, **6**, 15-50.
3. J. P. Perdew, K. Burke and M. Ernzerhof, *Phys. Rev. Lett.*, 1997, **78**, 1396-1396.
4. P. E. Blöchl, *Phys. Rev. B*, 1994, **50**, 17953-17979.
5. S. Grimme, J. Antony, S. Ehrlich and H. Krieg, *J. Chem. Phys.*, 2010, **132**, 154104.
6. M. J. Frisch, G. W. Trucks, H. B. Schlegel, G. E. Scuseria, M. A. Robb, J. R. Cheeseman, G. Scalmani, V. Barone, G. A. Petersson, H. Nakatsuji, X. Li, M. Caricato, A. V. Marenich, J. Bloino, B. G. Janesko, R. Gomperts, B. Mennucci, H. P. Hratchian, J. V. Ortiz, A. F. Izmaylov, J. L. Sonnenberg, Williams, F. Ding, F. Lipparini, F. Egidi, J. Goings, B. Peng, A. Petrone, T. Henderson, D. Ranasinghe, V. G. Zakrzewski, J. Gao, N. Rega, G. Zheng, W. Liang, M. Hada, M. Ehara, K. Toyota, R. Fukuda, J. Hasegawa, M. Ishida, T. Nakajima, Y. Honda, O. Kitao, H. Nakai, T. Vreven, K. Throssell, J. A. Montgomery Jr., J. E. Peralta, F. Ogliaro, M. J. Bearpark, J. J. Heyd, E. N. Brothers, K. N. Kudin, V. N. Staroverov, T. A. Keith, R. Kobayashi, J. Normand, K. Raghavachari, A. P. Rendell, J. C. Burant, S. S. Iyengar, J. Tomasi, M. Cossi, J. M. Millam, M. Klene, C. Adamo, R. Cammi, J. W. Ochterski, R. L. Martin, K. Morokuma, O. Farkas, J. B. Foresman and D. J. Fox, *CT* 2016.
7. GaussView, Version 6, Dennington, Roy; Keith, Todd A.; Millam, John M. Semichem Inc., Shawnee Mission, KS, 2016.
8. Y. Zhao and D. G. Truhlar, *Acc. Chem. Res.*, 2008, **41**, 157-167.
9. M. J. Abraham, T. Murtola, R. Schulz, S. Páll, J. C. Smith, B. Hess and E. Lindahl, *SoftwareX*, 2015, **1-2**, 19-25.
10. A. W. Sousa da Silva and W. F. Vranken, *BMC Research Notes*, 2012, **5**, 367.
11. C. I. Bayly, P. Cieplak, W. Cornell and P. A. Kollman, *The Journal of Physical Chemistry*, 1993, **97**, 10269-10280.
12. M. Schauperl, P. S. Nerenberg, H. Jang, L.-P. Wang, C. I. Bayly, D. L. Mobley and M. K. Gilson, *Comm. Chem.*, 2020, **3**, 44.
13. W. Humphrey, A. Dalke and K. Schulten, *J. Mol. Graph.*, 1996, **14**, 33-38.
14. L. Cao, D. Li, T. Pollard, T. Deng, B. Zhang, C. Yang, L. Chen, J. Vatamanu, E. Hu, M. J. Hourwitz, L. Ma, M. Ding, Q. Li, S. Hou, K. Gaskell, J. T. Fourkas, X.-Q. Yang, K. Xu, O. Borodin and C. Wang, *Nat. Nanotechnol.*, 2021, **16**, 902-910.
15. N. Chang, T. Li, R. Li, S. Wang, Y. Yin, H. Zhang and X. Li, *Energy Environ. Sci.*, 2020, **13**, 3527-3535.
16. N. Yao, S.-Y. Sun, X. Chen, X.-Q. Zhang, X. Shen, Z.-H. Fu, R. Zhang and Q. Zhang, *Angew. Chem. Int. Ed.*, 2022, **61**, e202210859.
17. B. Niu, Z. Li, D. Luo, X. Ma, Q. Yang, Y.-E. Liu, X. Yu, X. He, Y. Qiao and X. Wang, *Energy Environ. Sci.*, 2023, **16**, 1662-1675.
18. H. Zhang, Y. Zhong, J. Li, Y. Liao, J. Zeng, Y. Shen, L. Yuan, Z. Li and Y. Huang, *Adv. Energy Mater.*, 2023, **13**, 2203254.
19. Y. Wang, Z. Wang, W. K. Pang, W. Lie, J. A. Yuwono, G. Liang, S. Liu, A. M. D. Angelo, J. Deng, Y. Fan, K. Davey, B. Li and Z. Guo, *Nat. Commun.*, 2023, **14**, 2720.
20. Y. Lv, M. Zhao, Y. Du, Y. Kang, Y. Xiao and S. Chen, *Energy Environ. Sci.*, 2022, **15**, 4748-4760.
21. C. Huang, X. Zhao, Y. Hao, Y. Yang, Y. Qian, G. Chang, Y. Zhang, Q. Tang, A. Hu and X. Chen, *Energy Environ. Sci.*, 2023, **16**, 1721-1731.
22. Y. Wang, B. Liang, J. Zhu, G. Li, Q. Li, R. Ye, J. Fan and C. Zhi, *Angew. Chem. Int. Ed.*, 2023, **62**, e202302583.
23. P. Xiao, Y. Wu, J. Fu, J. Liang, Y. Zhao, Y. Ma, T. Zhai and H. Li, *ACS Energy Lett.*, 2023, **8**, 31-39.
24. Y. Zhao, M. Ouyang, Y. Wang, R. Qin, H. Zhang, W. Pan, D. Y. C. Leung, B. Wu, X. Liu, N. P. Brandon, J. Xuan, F. Pan and H. Wang, *Adv. Funct. Mater.*, 2022, **32**, 2203019.
25. C. Lin, X. Yang, P. Xiong, H. Lin, L. He, Q. Yao, M. Wei, Q. Qian, Q. Chen and L. Zeng, *Adv. Sci.*, 2022, **9**, 2201433.
26. C. Huang, X. Zhao, S. Liu, Y. Hao, Q. Tang, A. Hu, Z. Liu and X. Chen, *Adv. Mater.*, 2021, **33**, 2100445.
27. Y. Lin, Z. Mai, H. Liang, Y. Li, G. Yang and C. Wang, *Energy Environ. Sci.*, 2023, **16**, 687-697.
28. K. Guan, L. Tao, R. Yang, H. Zhang, N. Wang, H. Wan, J. Cui, J. Zhang, H. Wang and H. Wang, *Adv. Energy Mater.*, 2022, **12**, 2103557.
29. X. Yang, W. Li, Z. Chen, M. Tian, J. Peng, J. Luo, Y. Su, Y. Zou, G. Weng, Y. Shao, S. Dou and J. Sun, *Angew. Chem. Int. Ed.*, 2023, **62**, e202218454.
30. X. Zhang, Z. Deng, C. Xu, Y. Deng, Y. Jia, H. Luo, H. Wu, W. Cai and Y. Zhang, *Adv. Energy Mater.*, 2023, **13**, 2302749.